

Advances in phase-stepping real-time holography using photorefractive sillenite crystals

M. R. R. GESUALDI^a, E. A. BARBOSA^{b*}, M. MURAMATSU^c

^a*Instituto de Pesquisa e Desenvolvimento, Universidade do Vale do Paraíba, Av. Shishima Hifumi, 2911, Urbanova, CEP12244-000, São José dos Campos – SP, Brazil*

^b*Laboratório de Óptica Aplicada, Faculdade de Tecnologia de São Paulo, CEETEPS-UNESP, Pça Cel Fernando Prestes, 30, CEP 01124 060, São Paulo – SP, Brazil*

^c*Instituto de Física, Universidade de São Paulo, Rua do Matão, Travessa R, 187. CEP 05508-900, Cid.Universitária, São Paulo - SP – Brazil*

This work presents a review of recent developments in phase-stepping real-time holographic interferometry with photorefractive sillenite crystals. Quantitative results are shown in micro-rotation, micro-displacement, and micro-deformation measurements, and in wave-optics and surface analysis as well. The phase stepping was carried out in a four-frame process and the resulting phase map was unwrapped by applying a sin/cos filter. The experimental results are in good agreement with the ones obtained through other means, showing the promising potentialities of phase-stepping real-time holographic interferometry for *in situ* visualisation, monitoring and analysis in non-destructive testing.

(Received June 7, 2006; accepted July 20, 2006)

Keywords: Holography, Interferometry, Phase shifting

1. Introduction

Holographic interferometry comprises a group of powerful optical methods for non-destructive testing with many applications in basic research, biomedicine and technological areas [1]. Those techniques present important advantages over the conventional ones: they do not present any contact with the studied surfaces, providing absolute reliability and high accuracy; moreover, holographic interferometry allows an accurate qualitative analysis through visual inspection.

Several works reported the employ of photorefractive crystals (PRCs) in holographic interferometry throughout the last decades, since many interesting properties qualify them as recording media for real-time holographic interferometry (RTHI) [2,3,4]. The light-induced mechanisms that characterise the holographic grating buildup in these crystals are the photorefractive effect, the thermo-optic refractive index modulation and the photochromic effect. The first effect consists on the refractive index modulation through photo-induction and linear electro-optic effect (Pockels effect); the refractive index modulation by thermo-optic effects is due to temperature gradients on the crystal surface; the latter effect is caused by absorption coefficient modulation for high light intensities. The use of these crystals in photorefractive holographic recording present advantages like *in situ* self-proceeding of recording medium and indefinite reusability. Moreover, PRCs do not present fatigue in dynamic and reversible processes. Photorefractive crystals of the sillenite family such as Bi₁₂SiO₂₀ (BSO), Bi₁₂TiO₂₀ (BTO) and Bi₁₂GeO₂₀ (BGO) particularly present very interesting properties for RTHI. Despite their lower gain if compared with other materials like BaTiO₃ and LiNbO₃, they present a much faster hologram build up and provide less noisy holographic

images due to their anisotropic diffraction properties, through which the transmitted object wave is cut-off thus enabling the readout of the diffracted wave only [4]. Those properties enabled studies on vibration analysis [5,6,7,8], stress and deformation measurement [9,10], and material characterisation [11].

Spatial phase measurements are basically accomplished by changing the interferogram intensity. The phase shifting process consists on the acquisition of many interferograms which have their intensities changed by continuous, linear mirror micro-displacements. On the other hand, the phase stepping technique (PST) is based on discrete phase shifts. Many works contributed to the field of holographic interferometry by phase-shifting methods with photorefractive crystals. Georges and Lemaire with BSO [12] and Dirksen *et al* [13] with BTO crystals used argon ion lasers as light source and the Carré phase shifting method for interferogram evaluation in deformation and displacement measurements. Millerd and Brock with BaTiO₃ and diode lasers in the infrared region [14], Barbosa *et al* with BTO and red multimode diode lasers [15] and Gesualdi *et al* with BSO [16] performed surface analysis by holographic interferometry using four-frame phase-stepping methods for fringe evaluation. Labrunie *et al* [17] performed real-time quantitative measurement by means of a BSO-based holographic setup using the polarisation properties of holographic recording in sillenite crystals and two CCD cameras for displacement measurement.

After obtaining the phase map, phase unwrapping algorithms provide a complete quantitative description of the studied phenomena [18]. Along the years, many works on unwrapping techniques have been published [19,20,21,22,23], aiming applications in technological and biomedical areas.

The aim of this work is reviewing the recent achievements on the theoretical description and the experimental development of the phase stepping technique applied to real-time holography with sillenite crystals in areas like dynamic phenomena analysis, surface analysis and wave optics. Concerning that, this paper is organised as follows: in Section 2 we present a brief theoretical description of the four-frame PST applied to double-exposure holographic interferometry for displacement measurement and wave optics. In Section 2.3.3 we describe the use of PST in two holographic techniques of surface profiling, namely the rotation-source method and multi-wavelength holography. In the experiments (Section 3) we describe the procedures for holographic recording optimization and measurement calibration. The displacement and deformation analysis and the wave optics analysis as well are shown in Section 3.2; the surface analysis is shown in Section 3.3.

The optimised holographic interferometer using a $\text{Bi}_{12}\text{SiO}_{20}$ photorefractive crystal for micro-displacement and micro-rotation measurement is described in Section 3.1. The optical setup is connected to a interferogram analysis system for quantitative evaluation. In the experiments the interferograms were obtained by using a temporal controller of recording-reading process and the phase map was calculated by the four-frame PST. Another algorithm was then applied for phase map unwrapping. Results in good agreement with measurements by other techniques were obtained in many cases: measurements of micro-rotation of surfaces, punctual micro-displacements of an aluminium plate, deformation in a jaw of a dog and a dental implant screw. We presented also the possibilities of wave-optics analysis by phase-stepping real-time holographic interferometry. The quantitative evaluation of the intensity and phase distribution of the wavefronts generated by two types of lenses presented in this paper has the advantage of allowing the investigation of geometrical and diffraction effects.

In the section dedicated to surface analysis through the PST by holography with BSO and BTO crystals, we show that phase stepping interferometry can be successfully employed [14]. Holographic surface contouring presents interesting characteristics like noncontacting, whole-field, high-resolution measurements with many applications in biotechnology and engineering [24,25,26,27]. There are different holographic contouring methods, including sandwich holography, two-index method, two-wavelength method, two-source method and rotation-source method. The basic principle of holographic contouring lays on the generation of interference fringes corresponding to planes of constant elevation. In this paper we employed two methods for PST-based holographic profilometry in sillenite crystals, the rotation source method and the multi-wavelength holographic recording. In the first, contour fringes are generated through double exposure by tilting the object illumination beam [28]; in the latter, multiple holograms are simultaneously recorded in the storage medium by using multimode diode lasers [29]. The contour fringes arise from the phase difference between waves diffracted by different holograms.

All real-time holographic processes considered in this work occur in a diffusive regime (with no externally

applied electric field) and the sillenite crystals are oriented and cut in the electrooptic transverse configuration in order to explore their anisotropic diffraction properties [4]. For phase map unwrapping, sinusoidal filters were applied. The surfaces of many objects present real discontinuities and the experimental results agree with conventional measurements or with the actual object shape.

2. Theory

2.1 Real-time Holography using photorefractive sillenite crystals

In real-time holographic interferometry (RTHI) the hologram is recorded, and during the readout process the object is also illuminated. Since the hologram and the object remain in their original positions, the resulting image is the superposition of the holographically reconstructed object wavefront and the wavefront coming directly from the object. Each perturbation on the object produces fringes on its image due to the interference between the diffracted wavefront and the modified object wavefront.

Let us consider the incidence of two coherent monochromatic waves onto a sillenite crystal. For holographic recording by diffusion, the hologram diffraction efficiency is given by [30]

$$\eta = \left(\frac{\pi \Delta n}{\lambda \cos \theta} \frac{\sin \rho L}{\rho L} \right)^2 m^2 \quad (1)$$

where λ is recording wavelength, ρ is the crystal rotatory power, L is the crystal thickness, m is the modulation of the incident interference pattern and 2θ is the angle between the interfering beams. The refractive index modulation of the hologram is written as $\Delta n = n_o^3 r_{41} E_{sc} / 2$, where n_o is the refractive index, r_{41} is the linear electro-optic coefficient of the sillenite crystal and E_{sc} is the electric field generated by the redistributed space charges in the crystal. If τ is the hologram response (build-up or erasure) time, the light intensity I_0 at a point (x, y) resulting from the overlap of the wave diffracted by the hologram with the transmitted wave coming directly from the object is given by [28]

$$I_0(x, y) = I_{0,T}(x, y) + I_{0,D}(x, y) [1 - e^{(-t/\tau)}]^2 \quad (2)$$

The term $I_{0,T}(x, y)$ is the transmitted object wave and $I_{0,D}(x, y)$ is the holographic reconstruction of the object wave. The latter is written as

$$I_{0,D}(x, y) = I_{0,O}(x, y) \eta + I_{0,R}(x, y) [1 - \eta] + 2gY \cos \Phi \quad (3)$$

In the relation above, $I_{0,O}(x, y)$ and $I_{0,R}(x, y)$ are the object beam and the reference beam intensities, respectively, g is

a parameter expressing the polarisation coupling of both beams, $Y \equiv [\eta(1-\eta)I_{0,o}(x,y)I_{0,r}(x,y)]^{1/2}$ is the interference term and Φ is the phase shift on the object beam.

2.2 Phase-stepping technique

The interferogram phase map can be determined by capturing a sequence of four frames. Between each pair of frames a $\pi/2$ -phase change is introduced in the reference beam, thus changing the interferogram intensity. The intensity of the n -th interferogram $I_{0n}(x,y)$ at the point (x,y) is written as:

$$I_{0n}(x,y) = I_0(x,y) \cos^2 \left[\Phi(x,y) + \frac{(n-1)\pi}{2} \right] \quad (4)$$

$n=1,2,3,4$

By employing trigonometric relations and combining the intensities one obtains the phase $\Phi(x,y)$:

$$\Phi(x,y) = \arctan \left[\frac{I_{04}(x,y) - I_{02}(x,y)}{I_{01}(x,y) - I_{03}(x,y)} \right] \quad (5)$$

As the frames are acquired the hologram starts erasing, leading to a temporal decrease of the interferogram visibility according to $\exp(-t/\tau)$. In the experiments this can be overcome by shortening the acquisition time and thus making this variation negligible. For this reason the variation of the interferogram visibility in equations (4) and (5) was neglected. In reference [12] the measurement error due to the hologram erasure time was quantitatively analysed and the optimal value of τ which does minimise such error was determined.

By calculating the phase $\Phi(x,y)$, a 2-D phase map is built and the phase of a given point is represented in a gray level diagram. The 256 gray levels are a measure of values between $-\pi$ (black) and π (white) distributed in an image system of 8 bits. The resulting wrapped pattern looks like a border extending from white to black or from black to white. This phase modulation can be removed through several so-called unwrapping methods. In this work the color unwrapping phase map was obtained through the Branch-Cut Method [31].

2.3 Applications

2.3.1 Micro-Displacements and Micro-Deformations

Fig. 1 shows the optical setup for micro-displacement and micro-deformation measurement of opaque objects by RTI through the phase stepping technique. The displacement or deformation d at the point (x,y) can be written as [22]:

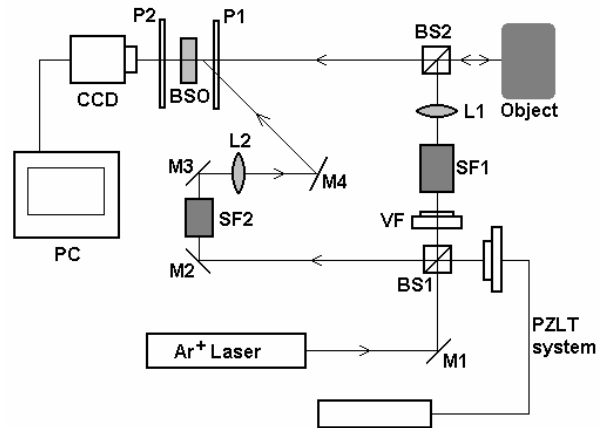


Fig. 1. Real-Time holographic setup with photorefractive BSO crystals; the light source is an Argon Laser ($\lambda = 514,5 \text{ nm}$); M1, M2, M3 and M4 are plane mirrors; BS1 and BS2, beam-splitters; SF1 and SF2, spatial filters; L1 and L2, lenses; P1 and P2, polarisers; PZLT, piezoelectric system; BSO, photorefractive crystal; CCD, camera; PC, computer.

$$d(x,y) = \frac{\Phi(x,y)(\cos \vartheta \cos \vartheta')}{k(\cos \vartheta + \cos \vartheta')} \quad (6)$$

where ϑ and ϑ' are the object illumination and observation angle, respectively and $k \equiv 2\pi/\lambda$. In our setup $\vartheta = \vartheta' = 0$, thus $d(x,y) = \Phi(x,y)/2k$.

2.3.2 Wave-optics analysis

In wave-optics analysis for lens evaluation the interferometric methods are usually employed. The Twyman-Green and Mach-Zehnder interferometers are the most popular in classical wave aberration measurements. In our case, we use holographic interferometry combined to the phase-stepping technique for detecting phase variations in the wavefront across a plane immediately behind the lens. This analysis is in accordance with geometrical optics, with the additional advantage that in the wave optics approach diffraction effects are completely accounted for.

The lens simply delays an incident wavefront by an amount proportional to its thickness at each wavefront point. The total phase delay suffered by the wave at coordinates (x,y) by passing through a lens may be represented as a multiplicative phase transformation of the form $t_L(x,y)$. The complex field $U'_L(x,y)$ across a plane immediately behind the lens is then related to the complex field $U_L(x,y)$ incident on a plane immediately at the lens input by

$$U'_L(x, y) = t_L(x, y)U_L(x, y) \quad (7)$$

The physical meaning of the lens transformation can be best understood by considering the effect of the spherical lens on a normally incident, unit-amplitude plane wave. Hence, the lens transformation $t_L(x, y)$ is described by

$$\begin{aligned} t_L(x, y) &= \exp[-i\Phi(x, y)] \\ &= \exp\left[-i\frac{\pi}{\lambda f}(x^2 + y^2)\right] \end{aligned} \quad (8)$$

Considering the input field distribution as unitary, the field after the lens can be written as:

$$U'_L(x, y) = \exp\left[-i\frac{\pi}{\lambda f}(x^2 + y^2)\right] \quad (9)$$

where f is the focal length of the lens.

2.3.3 Surface contouring

2.3.3.1 Rotation-source method

For surface measurement we take the difference between the reconstructed phases recorded before and after a small tilt $\Delta\alpha$ of the object illuminating beam. Between the acquisitions of the phase-shifted interference patterns the mirror M_{tilt} is rotated by an angle $\Delta\alpha/2$ from the initial angle of incidence α shown in the detail of the optical setup in figure 2.

In this section we basically follow the description made by Pedrini *et al* [27] and Yamaguchi *et al* [32]. Let us consider a 2-D analysis parallel to the table top (xz -plane) after the mirror rotation. Taking a point (x, y) on the object surface, the phases $\phi_{x,y}$ and $\phi'_{x,y}$ with respect to an arbitrary point before and after the mirror tilt are respectively expressed by

$$\phi_{x,y} = k|X \sin\alpha + Z \cos\alpha| \quad (10)$$

and

$$\phi'_{x,y} = k|X \sin(\alpha + \Delta\alpha) + Z \cos(\alpha + \Delta\alpha)|, \quad (11)$$

where X and Z are the x - and z -components of the position vector from point (x, y) to an arbitrary point located in the xz -plane with height y . The phase difference $\Phi = \phi_{x,y} - \phi'_{x,y}$ due to the mirror tilt is thus written as

$$\begin{aligned} \Phi &= 2k \sin\left(\frac{\Delta\alpha}{2}\right) \times \\ &\left| X \cos\left(\alpha + \frac{\Delta\alpha}{2}\right) - Z \sin\left(\alpha + \frac{\Delta\alpha}{2}\right) \right| \end{aligned} \quad (1)$$

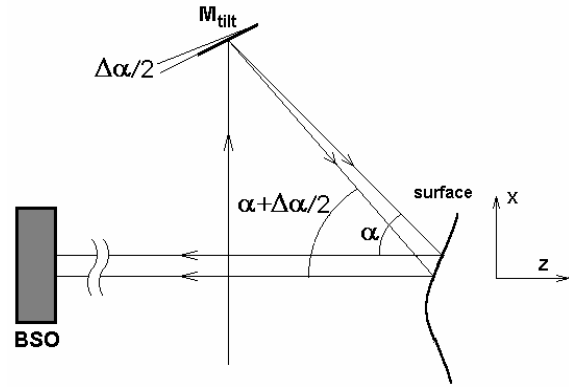


Fig. 2. Detail of the optical setup showing the incidence of the illuminating beam onto the object for surface profiling.

For the point (x', y') laying on the next interference fringe equation (12) yields

$$\begin{aligned} \Phi + 2\pi &= 2k \sin\left(\frac{\Delta\alpha}{2}\right) \times \\ &\left| X' \cos\left(\alpha + \frac{\Delta\alpha}{2}\right) - Z \sin\left(\alpha + \frac{\Delta\alpha}{2}\right) \right| \end{aligned} \quad (13)$$

From equations (12) and (13) one obtains the distance ΔX between the planes intersecting the object surface:

$$\begin{aligned} \Delta X &= (X - X') \cos\left(\alpha + \frac{\Delta\alpha}{2}\right) \\ &= \frac{\lambda}{2 \sin(\Delta\alpha/2)} \cong \frac{\lambda}{\Delta\alpha} \end{aligned}, \quad (14)$$

for small tilt angles. The length ΔX is perpendicular to the illuminating beams, thus the fringe pattern is generated by the intersection of the surface with the planes parallel to the bisector of those beams.

By keeping x constant, a similar approach provides the contour sensitivity $\Delta\Gamma$:

$$\begin{aligned} \Delta\Gamma &= (Z' - Z) \sin\left(\alpha + \frac{\Delta\alpha}{2}\right) \\ &= \frac{\lambda}{2} \left[\sin\left(\frac{\Delta\alpha}{2}\right) \sin\left(\alpha + \frac{\Delta\alpha}{2}\right) \right]^{-1} \cong \frac{\lambda}{\Delta\alpha \sin\alpha} \end{aligned} \quad (15)$$

Since the generated interference pattern is of \cos^2 -type, the phase stepping technique can be applied by substituting the phase Φ from equation (12) in equations (4) and (5).

Compared with the traditional two-wavelength method, the rotation source method is simpler, and the sensitivity is the same as resulting from the conventional fringe projection method.

2.3.3.2 Multi-wavelength Holography

In multi-wavelength holography both the object and the reference beams originate from a multimode diode

laser. Such inhomogeneously broadened laser emits simultaneously several longitudinal modes due to effects like spectral hole burning and spatial hole burning. The free spectral range (FSR) of the emission is inversely proportional to the laser resonator length in both effects.

According to the analysis of references [15,29], for N oscillating laser modes the reference and the object beams R_N and S_N at the sillenite crystal input have their amplitudes written as

$$R_N = R_0 \sum_{l=-(N-1)/2}^{l=(N-1)/2} A_l \exp\{i[(\bar{k} + l\Delta k)\Gamma_R + \phi_l]\} \quad (16)$$

$$S_N = S_0 \sum_{l=-(N-1)/2}^{l=(N-1)/2} A_l \exp\{i[(\bar{k} + l\Delta k)\Gamma_S + \phi_l]\}$$

where $\bar{k} \equiv 2\pi/\bar{\lambda}$ is the wavenumber for the central emission wavelength $\bar{\lambda}$, Δk is the wavenumber difference between two adjacent laser modes and Γ_S and Γ_R are the optical paths of the object and the reference beams, respectively. The real coefficient A_l is related to the intensity of each mode. The space charge electric field in equation (2) can be written as

$$E_{sc} \equiv iE_D \frac{2R^* S}{I_o} \quad (17)$$

where E_D is the diffusion electric field and I_o is the total light intensity incident onto the crystal. The superscript * denotes complex conjugation. From equations (1), (16) and (17) the hologram diffraction efficiency η_M for multi-wavelength holography can be given by

$$\eta_M = \eta \left| \sum_{l=-(N-1)/2}^{l=(N-1)/2} A_l^2 e^{i l \Delta k (\Gamma_S - \Gamma_R)} \right|^2 \quad (18)$$

For obtaining the equation above, it was considered that different modes do not interfere, since they are not mutually coherent. Thus, the terms containing the phase difference $\phi_l - \phi_m$ were neglected. Using the reference beam of intensity I_R as the readout beam, the intensity of the holographically reconstructed reference beam can be written as $I_S = \eta_M I_R$. Hence, the object reconstruction is written as

$$I_S = \eta \left| \sum_{l=-(N-1)/2}^{l=(N-1)/2} A_l^2 e^{i l \Delta k (\Gamma_S - \Gamma_R)} \right|^2 I_R \quad (19)$$

By taking $A_l = 1$ as the simplifying assumption that all modes oscillate with the same intensity, equation (17) takes the form

$$I_S = \eta \left\{ \frac{\sin[N\Delta k(\Gamma_S - \Gamma_R)/2]}{\sin[\Delta k(\Gamma_S - \Gamma_R)/2]} \right\}^2 I_R \quad (20)$$

The optical path of the reference beam Γ_R is constant and depends exclusively on the optical setup geometry. Since the beam illuminating the object and the beam scattered by it propagate in nearly opposite directions, Γ_S is related to the object surface height z as $\Gamma_S \cong 2z$. By setting arbitrarily $\Gamma_R = 0$, the intensity of the holographic image is written by

$$I_S = \eta \left[\frac{\sin(N\Delta kz)}{\sin(\Delta kz)} \right]^2 I_R \quad (21)$$

From the equation above one sees that bright and dark interference fringes cover the holographic image: the bright fringes correspond to regions on the surface for which

$$z = 2\pi q / \Delta k, \quad \text{while}$$

$z = 2\pi(q + 1/2) / \Delta k$ ($q = 0, 1, 2, 3, \dots$) is the region of the dark fringes. Hence, each bright or dark fringe define a plane of constant elevation, and the quantitative evaluation of the resulting interferogram provides the relief of the object surface. The height difference between two adjacent planes is given by $\Delta z = 2\pi / \Delta k$, and the surface analysis was accomplished by the four-frame PST. In analogy to equation (4), the intensity of each frame is obtained from equation (18) as

$$I_{S,n} = \eta \left\{ \frac{\sin[N(\Delta kz + (n-1)\pi/2)]}{\sin[\Delta kz + (n-1)\pi/2]} \right\}^2 I_R, \quad (22)$$

$n = 1, 2, 3 \text{ and } 4$

The diode laser used in the experiments of this work emits $N \cong 3$ modes, so that from equation (22) one obtains the surface height z for each point (x, y) on the surface [15]:

$$\Delta kz \cong \arctan \left(\frac{I_{S2}(x, y) - I_{S4}(x, y)}{I_{S1}(x, y) - I_{S3}(x, y)} \right) \quad (23)$$

The main advantage of the multi-wavelength method is that each interferogram can be obtained in single-exposure recordings. This provides fringe patterns without the need of intermediate steps like laser tuning or double-exposure processes. Thus, interferograms with equal visibility are easily obtainable throughout the whole phase-stepping process.

3. Experiments and results

3.1. RTHI optimization procedure

We used the experimental setup for RTHI by PST with photorefractive $\text{Bi}_{12}\text{SiO}_{20}$ (BSO) sillenite crystals as the recording medium shown in figure 1. The crystal was cut in the transverse electro-optic configuration with dimensions $10 \times 10 \times 3 \text{ mm}^3$. The recording laser beam is a cw Argon ion laser emitting at $\lambda = 514.5 \text{ nm}$ with 300 mW of output power. This light source was chosen because of the high sensitivity of BSO crystal for this wavelength. The recording laser beam was collimated and divided into

reference and object beams with equal optical paths. The acquisition of digital holographic images was made with a CCD camera connected to a microcomputer with a frame grabber. The processing system was performed with phase-stepping and processing software.

First, we evaluated the conditions in which the BSO crystal presented optimal performance for real-time holographic interferometry by diffusion. The optimal holographic recording angle θ was determined in order to maximise the diffraction efficiency η and minimise the response time τ . The BSO crystal was placed between two polarisers for adjusting the intensities of the transmitted and diffracted beams in order to provide the best contrast of interference pattern in the CCD camera. Thus, the best conditions were achieved for θ ranging from 40° to 50° ; the response time was ~ 10 s, and the ratio of reference-to-object beams intensity was $I_{0,R}/I_{0,O} \approx 6$.

We used a piezoelectrically driven mirror (PZT), model PZL-015 and a Step Driver PZ-100 (Burleigh Inc) for controlling the phase variation of the reference beam. A previous calibration was necessary in order to reduce the errors generated in the phase-shifter system.

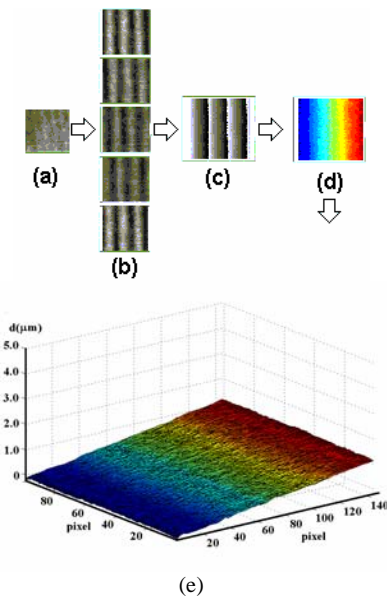


Fig. 3. Plane mirror micro-rotations: (a) holographic interferogram (160×160 pixels); (b) sequentially phase-shifted interferograms; (c) wrapped phase map; (d) color unwrapped phase map; (e) 3-D plot micro-rotation of $(1.2 \pm 0.3) \times 10^{-4}$ rad.

In order to test the repeatability and reliability of the system we performed a series of measurements using as object a plane mirror undergoing a rotation. This rotation was controlled by a micro-transducer and a rotation support, which provide a well-known and established set of rotation values. Fig. 3 illustrates the four-frame phase-stepping procedure for rotation measurement. Figure 3a shows the holographic image, Fig. 3b shows the interferograms obtained by phase shifting the reference beam, Fig. 3c and 3d are the wrapped and unwrapped phase maps, respectively, and Fig. 3e represents the 3-D

plot of the mirror rotation. Comparing the rotations measured by the four-frame PST with the values read from the mirror holder, it is possible to evaluate the system performance. As listed in references [12,17], the possible errors of the system are due to: 1. miscalibration of the phase-shifter; 2. spurious reflections and diffraction; 3. quality limitations of the optical elements; 4. nonlinearities and resolution of CCD; 5. air turbulence and vibrations, and photorefractive errors, like 6. temporal modulation of holographic interferograms and 7. Temporal fluctuation of thermal dependence on the photorefractive effect. Among them, the effects of air drift and undesired low-frequency vibrations during the holographic recording in a perturbed environment are the most prejudicial error source to the measurement accuracy [12] and to the holographic recording itself [6]. Such effects were minimised by mounting the holographic setup on a table top with pneumatic isolators and by performing the holographic recordings with no ambient air conditioning.

3.2. RTHI with phase-stepping technique applications

Rotation Measurements. With the optimised system, a series of measurements of the mirror rotation for different values of micro-rotations was made. One can measure values of micro-rotations in the range of 10^{-3} - 10^{-4} rad and the calculated values are in good agreement with the values read from micro-rotator. The results are shown in figures 3, 4 and 5.

Measurements of micro-displacements – the measurements of punctual micro-displacements in an aluminum plate are shown in figure 6. It was supported by a holder and a micrometric screw in order to produce a punctual displacement on the plate. The obtained value of the order of 10^{-4} mm, according to equation (6), is compatible with the values read from micrometer screw.

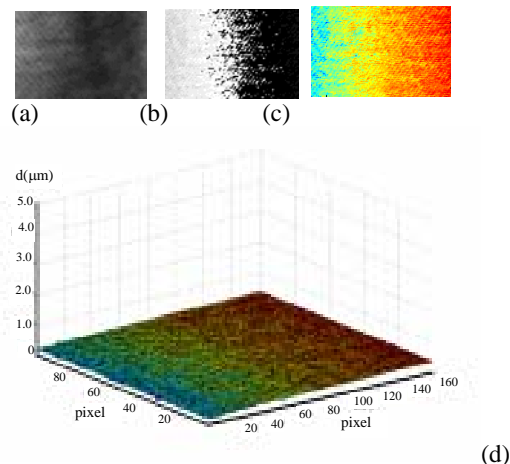


Fig. 4. Plane mirror micro-rotations: (a) holographic interferograms; (b) wrapped phase map; (c) color unwrapped phase map; (d) 3-D plot micro-rotation of $(9.4 \pm 0.2) \times 10^{-4}$ rad.

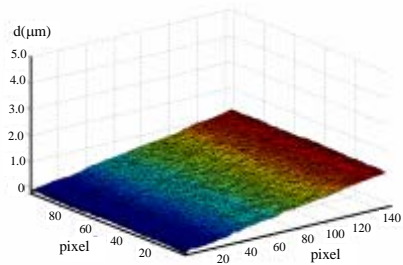


Fig. 5. 3-D plot of $(19.3 \pm 0.2) \times 10^{-4}$ – rad plane mirror micro-rotation .

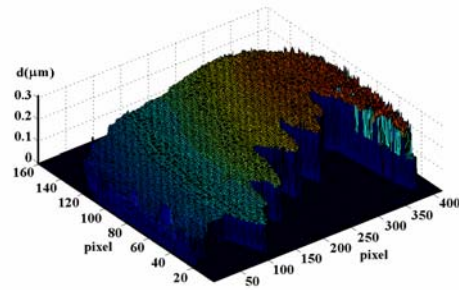


Fig. 8. 3-D plot of displacement of a dog jaw structure

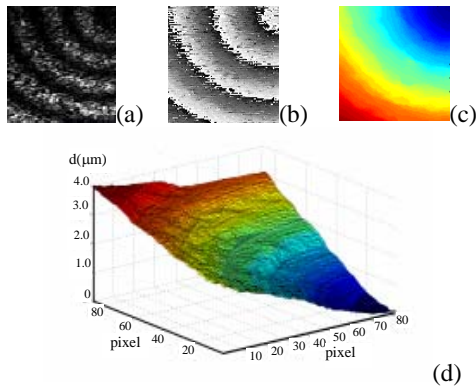


Fig. 6. Punctual displacement of an aluminum plate: (a) holographic interferogram; (b) wrapped phase map; (c) color unwrapped phase map; and (d) 3-D plot of the surface displacement.

Measurements of deformations for dentistry- first, the stress on a dental implant screw due to a mechanical load and the correspondent displacement values are shown in figure 7. The stress on a dog jaw due to a load applied on molar tooth was also analysed, as shows the 3-D plot in figure 8 [22].

Wave-optics analysis. The optical setup for wavefront reconstruction is basically the same as shown in figure 1 without a diffusely scattering light object. We first performed a holographic recording with a plane wave as the object beam. A spherical, positive test lens L_T with focal length $f = 50$ mm was then inserted into the object beam path and a second holographic exposure was performed. The holographic reconstruction presented the interference of the plane and the spherical waves with the typically circular, concentric interference fringes. By applying the four-frame phase stepping procedure the phase map of the wavefront generated by the spherical lens was obtained. Figures 9a-9d show the steps of the wavefront reconstruction for a 50-mm focal length spherical lens, while figure 10 shows the reconstructed wavefront for a 100-mm focal length cylindrical lens through the same analysis.

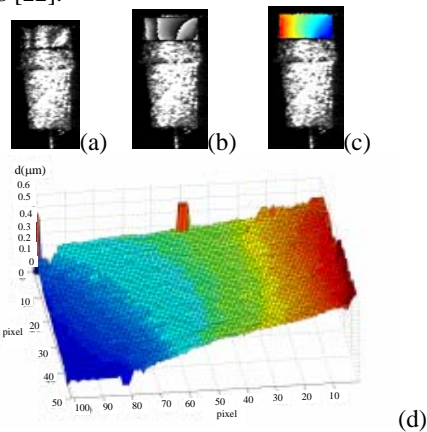


Fig. 7. Micro-displacement of dental implant screw: (a) interferogram; (b) wrapped phase map; (c) color unwrapped phase map; and (d) 3-D plot of displacement on surface.

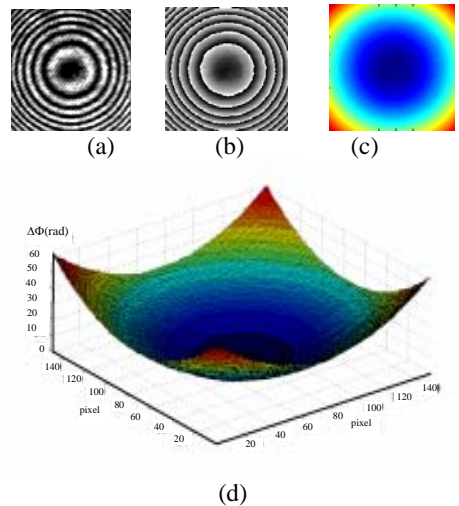


Fig. 9. Wavefront analysis for a $f= 50$ -mm spherical lens: (a) interferogram; (b) phase map; (c) unwrapped color phase map; (d) 3-D wavefront reconstruction.

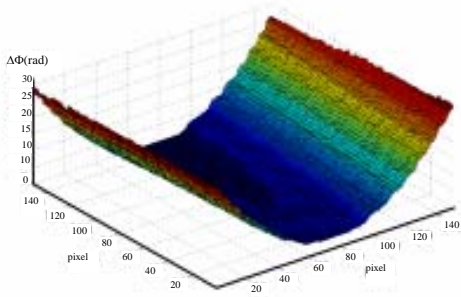


Fig. 10. 3-D wavefront reconstruction for a $f= 100\text{-mm}$ cylindrical lens.

3.3. Surface Contouring

Rotation-source method - the experimental setup used for surface contouring through the rotation source method is shown in Fig. 11. This is a variation of holographic setup in Fig. 1, with the insertion of the mirror M_{tilt} for tilting the illumination beam. The object was a plug of height 10.0 mm and diameter 20.0 mm measured with a caliper. The illumination-observation angle is $\alpha = 0.36$ rad and the tilt angle on the illumination beam was $\Delta\alpha = 6 \times 10^{-5}$ rad. The resulting interference contour fringes on the object surface are shown in Fig. 12a. By applying the four-frame PST and unwrapping processes, the surface analysis was carried out and the results are shown in Fig. 12b; these describe the internal border of the piece and are in good agreement with the actual surface relief.

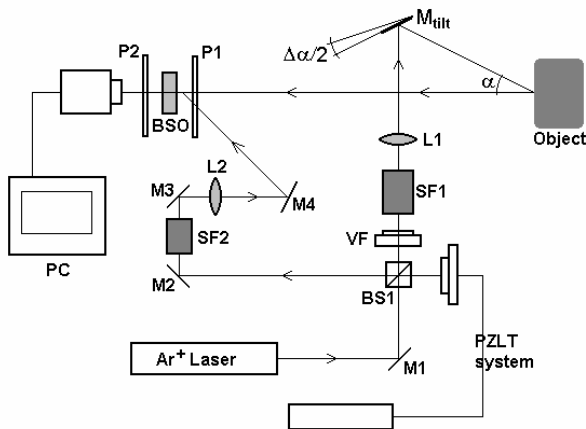
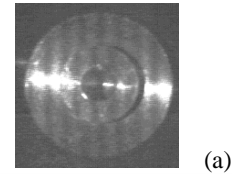
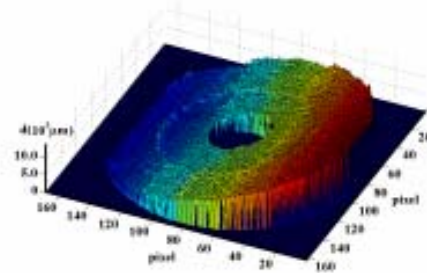


Fig. 11. Setup for surface contouring by the rotation source method.



(a)



(b)

Fig. 12. Surface analysis of a plug: (a) holographic interferogram (b) 3-D plot.

Multi-wavelength Holography. Fig. 13 shows the setup for surface relief study of a rigid object through holographic recording with a BTO crystal in diffusion regime using multi-mode laser. The object beam is collected by the lens L1, which forms the image at the BTO crystal, while the lens L2 builds the holographic object image at the CCD camera. In this case, the interference pattern on the holographic image is obtained exclusively from the diffracted wave, since the transmitted one is cut off by the analyzer P2 [4]. The 90-prism PR is mounted on a translation stage which introduces the phase-shift in the reference beam. We use as light source a 30-mW diode laser emitting around 670 nm with FRS $\Delta\nu = 53$ GHz, corresponding to $\Delta k = 1.18$ rad/mm and $\Delta z = 2.66$ mm. According to the holographic measurements performed in ref. [29], this laser emits in four modes with different intensities, i.e., $A_i \neq A_j$.

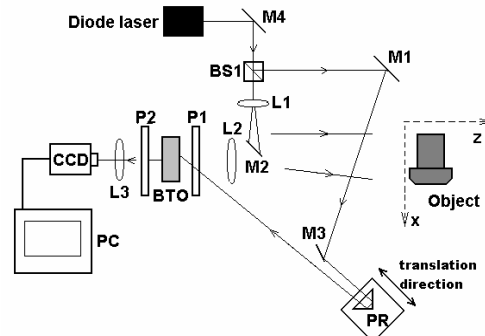


Fig. 13. Scheme of the optical setup for surface analysis by multimode lasers with a BTO crystal; PR is a 90°-prism.

In order to obtain the analytic solutions for the phase given by equations (22) and (23), we assume the oscillation of three equally intense laser modes, so that the intensity of the holographically reconstructed image is given by relation (21). As it will be seen later, this simplifying assumption provides very satisfactory results. We performed a single exposure in order to obtain the holographic image from a 15 X 25-mm² flat metallic plate, tilted $\sim 20^\circ$ with respect to the front face of BTO. The hologram recording time was ~ 10 s. The image of the object with the characteristic interference contour fringes is shown in Fig. 14a. Based on equation (23) the 3D scanning of the object can be accomplished by phase-stepping. For each step, the translation stage was displaced by $\Delta z/4 = 0.66$ mm. After the PST and unwrapping processes the surface relief is depicted in Fig. 14b, with an enlarged scale in the z-direction. From the data shown in this figure, the plate tilt angle was 20.5° , which is in excellent agreement with the tilt angle set in the optical setup ($\sim 20.3^\circ$).

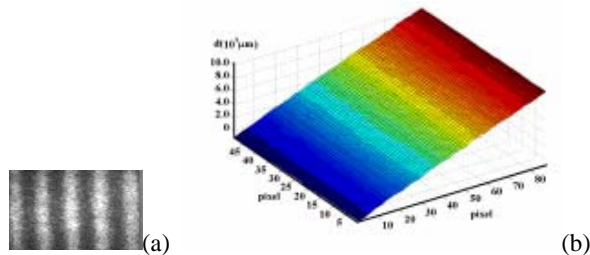


Fig. 14. Multi-wavelength surface analysis of a 30° -tilted flat bar: (a) interferogram; (b) 3-D plot.

The technique can also be applied to surfaces with different derivatives and textures. Figures 15a and 15b show the holographic interferogram and the resulting relief of a (partially illuminated) loudspeaker surface with diameter 7 cm [15], while figures 16a and 16b show the corresponding patterns of a tooth surface [33].

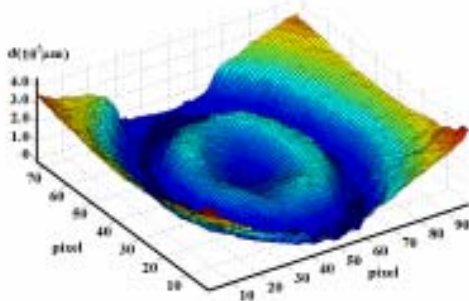


Fig. 15. 3-D plot of a loudspeaker by multi-wavelength holography.

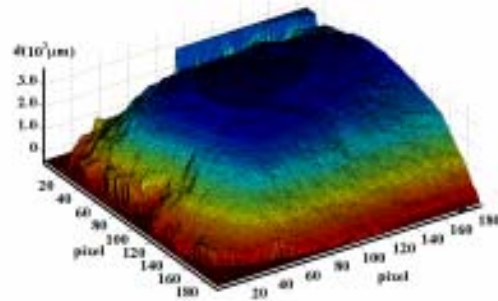


Fig. 16. 3-D plot of a tooth by multi-wavelength holography

4. Conclusions

This work presented a review of recent contributions to phase-stepping real-time holography using photorefractive sillenite crystals. Quantitative results in many applications such like measurements of micro-rotations, micro-displacements, micro-deformations, wave-optics and surface contouring analysis were obtained in real-time holographic processes. The application of the four-frame PST and the unwrapping algorithms enabled experimental results in good agreement with data obtained through conventional methods and the whole-field character of the interferograms allowed for accurate visual inspection. Promising potentialities of this method for studies with *in situ* visualization, monitoring and analysis in non-destructive testing were pointed out.

Acknowledgements

The authors are grateful to Augusto C. Lima from Faculdade de Tecnologia de São Paulo for fruitful discussions. This work was partially supported by Fundação de Apoio à Tecnologia.

References

- [1] C. M. Vest, *Holographic Interferometry*, Wiley, New York (1979).
- [2] P. Yeh, *Introduction to Photorefractive Nonlinear Optics*, Wiley, New York (1993).
- [3] P. Gunter, J. P. Huinard, *Photorefractive Effects and Materials I, Photorefractive Materials and Their Applications II*, Topics in Appl. Phys., Springer, Berlin (1988).
- [4] A. A. Kamshilin and M. P. Petrov, *Opt. Comm.* **53**, 23 (1985).
- [5] A. A. Kamshilin, A. Kasuso, Kh. Korrea, E. Moreno, A. Oliva, *Sov. Phys. Acoust.* **35**, 104 (1989).
- [6] E. A. Barbosa, J. Frejlich, V. V. Prokofief, N. J. H. Gallo, J. P. Andreetta, *Opt. Eng.* **33**, 2659 (1994).

- [7] E. A. Barbosa, M. Muramatsu, *Opt. Las. Tech.* **29**, 359 (1997).
- [8] M. P. Georges, Ph. C. Lemaire, *Opt. Comm.* **145**, 249 (1997).
- [9] A. A. Kamshilin, A. Oliva, E. Moreno, *Sov. Phys. Tech. Phys.* **35**, 742 (1990).
- [10] M. P. Georges, V. S. Scaufaire, Ph. C. Lemaire, *Opt. Mat* **18**, 49 (2001).
- [11] E. A. Barbosa, R. Verzini, J. F. Carvalho, *Opt. Comm.*, in press (2006).
- [12] M. P. Georges, Ph. C. Lemaire, *Appl. Opt.* **34**, 7497 (1995).
- [13] D. Dirksen, F. Matthes, S. Riehemann, G. von Bally, *Opt. Comm.* **134**, 310 (1997).
- [14] J. E. Millerd, N. J. Brock, *Appl. Opt.* **36**, 2427 (1997).
- [15] E. A. Barbosa, A. A. V. Filho, M. R. R. Gesualdi, B. G. Curcio, M. Muramatsu, D. Soga, *J. Opt. Soc. Am. A* **22**, 1 (2005).
- [16] M. R. R. Gesualdi, D. Soga, M. Muramatsu, *Opt. Las. Engng*, in press (2006).
- [17] L. Labrunie, G. Pauliat, J. C. Launay, S. Leidenbach, G. Roosen, *Opt. Comm.* **140**, 119 (1997).
- [18] K. Creath, J. Schmit, *Opt. Lasers Eng.* **24**, 365 (1995).
- [19] T. R. Judge, P. J. Bryanston-Cross, *Opt. Lasers Eng.* **24**, 199 (1994).
- [20] J. Strand, T. Taxt, *Appl. Opt.* **38**, 4333 (1999).
- [21] M. P. Georges, Ph. C. Lemaire, *Appl. Phys. B* **68**, 1073 (1999).
- [22] M. R. R. Gesualdi, D. Soga, M. Muramatsu, *Opt Las. Eng.* **44**, 56 (2006).
- [23] J. W. Goodman, "Introduction to Fourier Optics", MacGraw-Hill, San Francisco, CA (1968).
- [24] F. M. Kuchel, H. J. Tiziani, *Opt. Comm.* **38**, 17 (1981).
- [25] M. Yonemura, *Opt. Lett.* **10**, 3 (1985).
- [26] T. Endo, Y. Yasuno, S. Makita, M. Itoh, T. Yatagai, *Opt. Express* **13**, 695 (2005).
- [27] G. Pedrini, P. Fröning, H. J. Tiziani, F. M. Santoyo, *Opt. Comm.* **164**, 257 (1999).
- [28] M. R. R. Gesualdi, D. Soga, M. Muramatsu, *Opt. Las. Tech.*, in press (2006).
- [29] E. A. Barbosa, *Appl. Phys. B.* **80**, 345 (2005).
- [30] S. Mallick, D. Rouède, *Appl. Phys. B* **43**, 239 (1987).
- [31] B. Gutmann, H. Weber, *Appl. Opt.* **38**, 5577 (1999).
- [32] I. Yamaguchi, S. Ohta, J.-I Kato, *Opt. Las. Engng* **36**, 417 (2001).
- [33] E. A. Barbosa, M.R. Gesualdi, M. Muramatsu, *Proceedings of SPIE ICO20, Optical Information Processing*, 6027, 2005.

*Corresponding auhtor: ebarbosa@fatecsp.br